ELSEVIER

Biochimica et Biophysica Acta 1365 (1998) 373–384

BIOCHIMICA ET BIOPHYSICA ACTA
BBA

The triplet state of the FMO complex of the green sulfur bacterium *Prosthecochloris aestuarii* studied with single-crystal EPR

R.J.W. Louwe, T.J. Aartsma, P. Gast, R.J. Hulsebosch, H.M. Nan [1], J. Vrieze, A.J. Hoff *

Department of Biophysics, Huygens Laboratory, Leiden University, P.O. Box 9504, 2300 RA Leiden, The Netherlands

Received 16 January 1998; revised 19 March 1998; accepted 25 March 1998

Abstract

Triplet-electron paramagnetic resonance (EPR) spectra were obtained of single crystals of the FMO complex of the green sulfur bacterium *Prostecochloris aestuarii*. The experiments support the results presented in a previous paper (Louwe et al., J. Phys. Chem. 101 (1997) 11280), which showed that the experimental optical spectra of this pigment-protein complex are best reproduced by assuming that one bacteriochlorophyll (BChl 3) is energetically isolated and that this BChl is the triplet-carrying BChl of the FMO complex at cryogenic temperatures for low excitation density. When comparing the experimental and simulated data sets of the triplet-EPR spectra in single crystals, the best fit is obtained for two triplet states, one localized at BChl 3 and the other at BChl 1. The existence of two different triplet states is traced to the relatively high excitation power necessary to observe the small triplet-EPR signal of the FMO single crystals.

Keywords: FMO complex; Electron paramagnetic resonance, single-crystal; Bacteriochlorophyll *a*; Triplet state; (*Prosthechloris aestuarii*)

1. Introduction

The bacteriochlorophyll (BChl) *a* antenna complex of green sulfur bacteria (commonly referred to as the FMO complex) provides a well-defined model system to study energy transfer processes in photosynthetic systems. Thanks to its solubility in water the FMO complex is relatively easy to isolate and crystallize [1]. With X-ray spectroscopy the structure of the complex was determined to 1.9 Å resolution [2]. The complex consists of a trimer with C_3 symmetry, each subunit of the trimer containing seven BChl *a* molecules. The Q_Y region in the optical absorption spectrum at low temperatures shows significant structure. The linear-dichroic [3], circular-dichroic [1,4,5] and triplet-minus-singlet spectra [3,6] exhibit similar resolution.

In [7], we reported on exciton simulations for various optical steady-state spectra of the FMO complex, which provided an excellent match with the experimental spectra. Results of optically detected magnetic resonance (ODMR) experiments [6] indicated that, in terms of the exciton model, the transition to the lowest excited state within the manifold of excited states is dominated by the contribution of

* Corresponding author. Fax: +31 (71) 5275819
E-mail: Hoff@biophys.leidenuniv.nl
[1] Present address: Gist-Brocades, P.O. Box 1, 2600 MA Delft, The Netherlands.

0005-2728/98/$19.00
PII: S0005-2728(98)00089-9

a single BChl. This can be explained by a significantly lower site energy of this BChl compared to those of the other BChls. Furthermore, the triplet-minus-singlet (T−S) and linear-dichroic (LD)-(T−S) spectra indicated that the intermolecular (dipolar) interactions are smaller than assumed previously [8–10]. Based on these results, a minimal set of free parameters was found sufficient for a good simulation of the optical spectra. Most important, we were able to simultaneously reproduce the essential features of the absorption, LD, T−S and LD-(T−S) spectra by considering only the interactions within a single FMO subunit. We concluded that BChl 3 (numbering according to [2]) has the lowest site energy, while the largest dipolar interaction energy between two neighboring BChls within a subunit is 90 cm^{-1}.

After optical excitation to the manifold of excited states and subsequent relaxation to the lowest excited state, a number of the excitations will result in triplet state formation via intersystem crossing. Since the lowest excited singlet state seems to contain a major contribution of one energetically isolated BChl, at thermodynamic equilibrium the formation of the triplet state will preferentially take place at this particular BChl. Identification of the triplet-carrying molecule plays a key role in finding the parameter set for the exciton simulations described above that most accurately reproduces the experimental T−S and LD-(T−S) spectra [3,6]. Therefore, the determination of the optimal parameter set for these simulations is considerably aided by an independent identification of the triplet-carrying molecule.

Potentially, EPR spectroscopy of triplet states on single crystals provides accurate information on the orientation of the triplet dipolar tensor in the crystal coordinate frame. With a known crystal structure this information may lead to an unequivocal identification of the triplet-carrying molecule(s). An example of this approach is the work by Gast and Norris [11,12], who determined the location of the triplet state of the primary electron donor in reaction centers of *Rhodopseudomonas viridis* and *Rhodobacter sphaeroides* R26. These experiments benefitted from the strong spin polarization of the triplet sublevels, resulting from the mode of formation of the primary donor triplet state, viz. through radical recombination with a low-temperature yield close to unity. In the FMO complex, however, such experiments are considerably more complicated, because here the triplet state is generated by intersystem crossing from the excited singlet state, with considerably lower yield and spin polarization. Also, the number of possible sites is much larger in the FMO complex compared to the reaction center, which renders resolving the triplet-carrying molecule much more difficult.

The hexagonal crystals obtained for the FMO complex have the symmetry space group $P6_3$. The morphological long axis of the crystal coincides with the crystal $\vec{c}$ axis, while the morphological short axis of the crystal corresponds to either the crystal $\vec{a}$ or the $\vec{b}$ axis. Each unit cell contains two FMO trimers, with the individual C_3-symmetry axes oriented parallel to the crystal $\vec{c}$ axis. The two trimers are rotated 60° around their C_3-symmetry axis with respect to each other. The orientation of the crystal is defined by a set of successive rotations $\{\varphi,\xi,\zeta\}$, which describe the deviation from the initial positioning of the crystal in the laboratory frame. The various coordinate frames and angles are defined in Fig. 1. As in [13], we use a set of orthogonal angles $\{\varphi,\xi,\zeta\}$ instead of a set of Euler angles, so that the orientation of the crystal is directly related to the various rotations as they are performed in an experiment.

The triplet state is assumed to be localized at a specific BChl, i.e. at one of the seven BChls in each subunit of a trimer. The two FMO trimers per unit cell give rise to six BChls with a magnetically inequivalent orientation in the laboratory axes frame $\{\vec{x}_L\vec{y}_L\vec{z}_L\}$, and thus contribute differently to the triplet-EPR spectrum, assuming an equal probability of triplet state formation for each of those six BChls. For each BChl only the two $\Delta M_S = 1$ transitions contribute to the spectrum, because the $\Delta M_S = 2$ transition is not allowed and occurs at much lower magnetic field, yielding a maximum number of 12 resonances for a particular orientation of the crystal. In the experiments presented here, only crystal orientations are considered with the crystal $\vec{c}$ axis perpendicular to the magnetic field, B_0. For crystal orientations with the crystal $\vec{c}$ axis perfectly aligned along the laboratory $\vec{y}_L$ axis, there are only three BChls per unit cell with a magnetically inequivalent orientation, so that at most six different resonances

for a particular orientation of the crystal will be observed. The orientation of the crystal is then completely defined by the rotation angle φ of the crystal and as a result of the symmetry in the crystal, the EPR spectra will be identical after rotating the crystal 60°.

Identification of the triplet-carrying molecule is in principle possible by comparing experimental and simulated EPR rotation patterns. The large number of potential sites and the fact that the EPR amplitudes are expected to be small emphasize the necessity to accurately determine how well the EPR rotation patterns of the various sites can be resolved before a unique identification of the triplet-carrying molecule can be made with confidence. Therefore, we will also compare the simulated rotation patterns for different triplet-carrying molecules and consider the influence of misalignment of the crystal, represented by the rotation angles ξ and ζ (Fig. 1).

In EPR spectroscopy, a comparison of rotation patterns is often presented by comparing only the resonant B_0 values. For the experiments that we will present here, however, an overall comparison including the EPR amplitudes of two data sets is necessary. In addition to the small signals and the large number of possible sites, mounting the crystals inside a capillary tube (see Section 2) presents another complication when the various data sets are compared, because it necessitates that φ be treated as a free adjustable parameter. For these reasons, the degree of correlation between the two data sets A and B, commonly referred to as the linear correlation coefficient or Pearson's product moment, r, is calculated (see e.g. [14]):

$$r_{A,B} = \frac{\sum_{i,j}(I_A-\bar{I}_A)(I_B-\bar{I}_B)}{\sqrt{\sum_{i,j}(I_A-\bar{I}_A)^2\sum_{i,j}(I_B-\bar{I}_B)^2}} \qquad I = f(B_0^i,\ \varphi^{(j)}) \tag{1}$$

where I represents the EPR amplitude at a specific B_0 value and rotation angle φ of the crystal. The absolute value of the linear correlation coefficient can take any value between 0 (no correlation) and 1 (perfect correlation).

The advantage of comparing the experimental data sets and the simulated data set i by the correlation coefficient $r_{(exp,i)}$ is that it provides a quantitative measure for the likelihood that site i is the triplet-carrying molecule. Furthermore, large deviations between $r_{(exp,j)}$ and $r_{(i,j)}$ for *any* site j≠i would indicate significant discrepancies between theory and experiment.

2. Materials and methods

2.1. Experimental

The direct-detection EPR set-up was essentially as described in [16] and operated at a microwave fre-

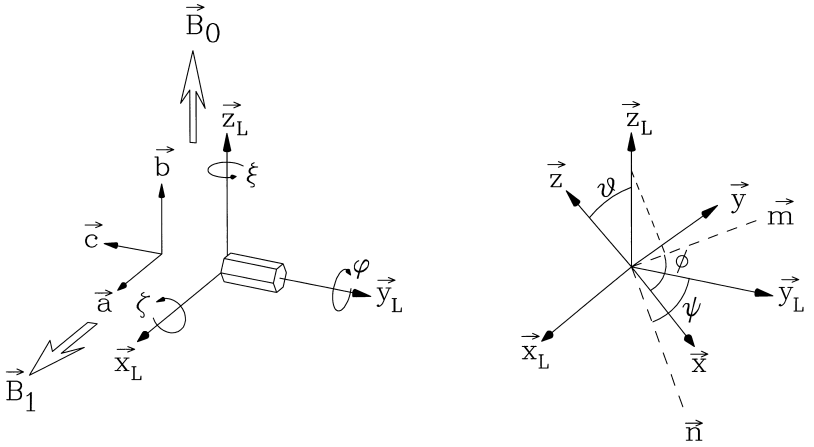

Fig. 1. Left: Definition of the angles φ, ξ and ζ relating the laboratory frame $\{\vec{x}_L\vec{y}_L\vec{z}_L\}$ and the crystal axes $\{\vec{a}\vec{b}\vec{c}\}$. Right: Euler angles θ, ϕ and ψ, which define the relation between the laboratory frame $\{\vec{x}_L\vec{y}_L\vec{z}_L\}$ and the molecular axis frame $\{\vec{x}\vec{y}\vec{z}\}$. The line n is the intersection between the $\vec{x}_L\vec{y}_L$ plane and the $\vec{x}\vec{y}$ plane and the line m is the projection of the laboratory z axis, $\vec{z}_L$, in the $\vec{x}\vec{y}$ plane.

quency of $\nu \approx 9.3$ GHz. An alternative detection scheme was used, however, to minimize the effect of the substantial detuning of the microwave cavity caused by the level of optical excitation necessary to observe an EPR signal in the experiments presented here.

Optimal improvement of the signal-to-noise ratio was obtained when two time windows of 5 μs were used, separated by 5 μs in time, in which the microwave intensity at the output of the microwave bridge was sampled with boxcar integrators. The first time window was used to detect the EPR signal, while the second time window was used to detect the (flash-induced) background signal. The signals were fed into a difference amplifier whose output was further processed as usual. The various scans (256 points, sweep time 2.5 min) were averaged 40 times for every orientation to further improve the signal-to-noise ratio. The EPR experiments were performed at 6 K in an Oxford EPR flow cryostat. The sample was excited with 15 ns laser pulses of 7.5 mJ at 810 nm using a BBO optical parametric oscillator pumped at 532 nm by a frequency-doubled Nd-YAG laser at a repetition rate of 10 Hz.

A Varian E-9 spectrometer, equipped with a multipurpose TE-101 cavity, was used to obtain the field-modulated triplet-EPR spectra. In addition to the field modulation (100 kHz), a 1.23 kHz light modulation was applied to remove signals persisting in dark-adapted samples, using a xenon light source (ILC Technology R300-5).

The FMO complex was isolated from *Prosteochloris aestuarii* following a procedure similar to that described by Miller et al. [17]. For experiments on the FMO complex in frozen solution, the samples were concentrated to an optical density of approximately 670 cm^{-1}, measured at the maximum of the Q_Y absorption band at room temperature, after which glycerol (50% v/v) was added to the sample. The FMO complex in frozen solution was contained in a standard 3 mm inside diameter EPR quartz tube, which was subsequently stored in liquid N_2 until further use.

Hexagonal crystals were grown as described in [18]. The quality of the crystals was visually inspected using a standard optical polarization microscope to check that the crystals displayed the optical birefringence associated with a well-ordered crystal [1]. At the intensity level of optical excitation necessary to detect the EPR signal, we lost the single crystals when mounted directly on the flat surface of the quartz rod. Therefore, the crystals were immobilized by vacuum insertion into a tapered capillary. The capillary was subsequently mounted on the quartz rod using a small drop of glycerol, which was quickly frozen using liquid N_2.

2.2. Simulations of the triplet-EPR spectra

The theory for calculating the triplet-EPR spectra has been extensively described in [19,20]. For full details of the theory we refer to these publications;

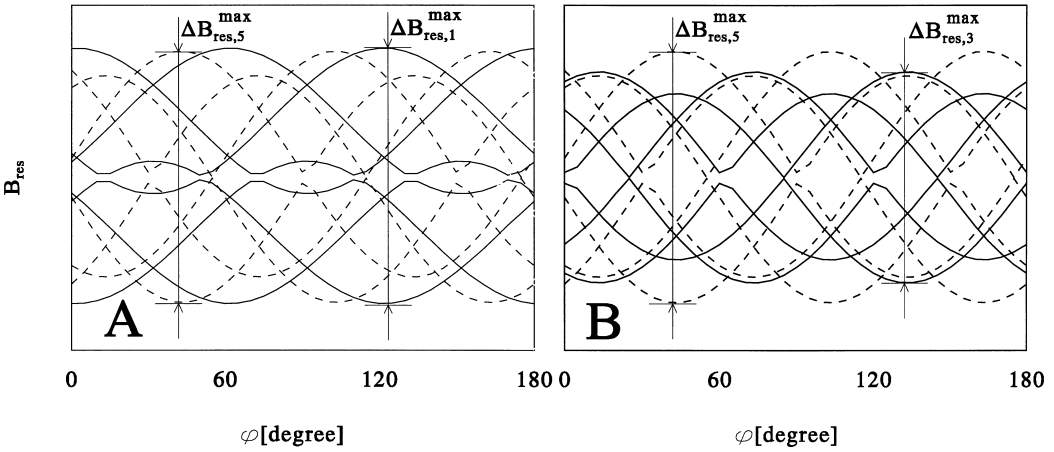

Fig. 2. Simulated B_{res} values as a function of the rotation angle φ for a triplet state located at various BChls. For each simulation the difference between the extreme B_{res} values, B^{max}_{res} is indicated. (A) Simulations of a triplet state located at BChl 1 (solid lines) or BChl 5 (dashed lines) yield almost identical B^{max}_{res} values. (B) Simulations of a triplet state located at BChl 3 (solid lines) or BChl 5 (dashed lines) yield distinct B^{max}_{res} values.

here we review only parts relevant for the present work.

The triplet-EPR spectra were simulated by first solving the secular equation of the high-field spin Hamiltonian, $H = \beta S.\mathbf{g}.B_0 - XS_x^2 - YS_y^2 - ZS_z^2$, with the first term the Zeeman interaction and X, Y, and Z the principal values of the triplet dipolar tensor of the molecule [15], to find the resonant B_0 values, B_{res}, for a specific orientation of a specific BChl in a subunit of the FMO complex. The principal axes $\{\vec{x}\,\vec{y}\,\vec{z}\}$ of the triplet dipolar tensor and the laboratory axis system $\{\vec{x}_L\,\vec{y}_L\,\vec{z}_L\}$ are related by the Euler angles θ, ϕ and ψ (see Fig. 1).

The relative intensity of a transition is calculated as the product of the population probability difference of the individual triplet sublevels, Δ, and the transition probability, W. The decay rates of the individual triplet sublevels are irrelevant if the EPR signal is detected immediately after the optical excitation using a boxcar integrator with a time gate much shorter than the lifetime of the triplet state (see Section 4, however) The population probabilities of the triplet sublevels in high field, p_k, are calculated from those in zero field, p_j:

$$p_k = \sum_j |C_{jk}|^2 \, p_j \quad (k = 1,2,3;\ j = x,y,z) \tag{2}$$

The coefficients C_{jk} represent the contribution of the zero-field eigenvectors τ_j to the high-field eigenfunction Φ_k, obtained from diagonalization of the spin Hamiltonian H:

$$\Phi_k = \sum_j \tau_j C_{jk} \quad (k = 1,2;\ j = x,y,z) \tag{3}$$

The transition probability W between high-field levels $|1\rangle$ and $|2\rangle$ is proportional to $|\langle\Phi_1|U.S|\Phi_2\rangle|^2$, where U is a unit vector in the direction of the oscillating microwave field, $\vec{B}_1$. Substitution of Eq. 3 in the above expression for W results in:

$$W = \sum_{i,j} \mu_i \mu_j (\vec{C}_1^* \wedge \vec{C}_2)_i (\vec{C}_1 \wedge \vec{C}_2^*)_j \quad (i,j = x,y,z) \tag{4}$$

where μ_i, μ_j are the direction cosines of $\vec{B}_1$ in the molecular frame $\{\vec{x}\,\vec{y}\,\vec{z}\}$, $\wedge$ represents a cross product, and $\vec{C}_k = \sum_j \vec{e}_j C_{jk}$ ($k = 1,2$, and $\vec{e}_j$ is a unit vector in the direction $j = \vec{x}, \vec{y}, \vec{z}$). For the simulation of the triplet-EPR spectra of single crystals, the procedure described above is repeated for each of the six equivalent BChls with a magnetically inequivalent orientation in the unit cell of the crystal, after which their individual contributions are added to form the total spectrum. The EPR spectrum of the FMO complex in frozen solution is simulated by summation of 45 triplet-EPR spectra of BChl *a* molecules with different, equally spaced orientations of $\vec{B}_0$ within an octant of the molecular frame $\{\vec{x}, \vec{y}, \vec{z}\}$.

The zfs parameters for the FMO complex that have been used in the simulations of the triplet-EPR spectra, $|D| = |-\frac{3}{2}Z| = 630$ MHz and $|E| = |-\frac{1}{2}(X-Y)| = 165$ MHz, were obtained from ODMR measurements [6,21]. The g-values are assumed to be identical to those observed for deuterated BChl a^+ in frozen solution: $g_{xx} = 2.0026$, $g_{yy} = 2.0033$, $g_{zz} = 2.0022$ [22]. In all simulations, values for the zero-field population probabilities of the individual triplet sublevels have been used that yield a good simulation of the experimentally observed triplet-EPR spectrum of the FMO complex in frozen solution: $p_x = 0.41$, $p_y = 0.59$, $p_z = 0$ (see Section 3). The calculated stick spectra were dressed with a Gaussian with linewidth of 2.25 mT (FWHM), representing inhomogeneous broadening.

2.3. Simulated single-crystal triplet-EPR spectra

The limited number of resonances (see Section 1) that are observed in the triplet-EPR spectra for $\vec{B}_0 \perp \vec{c}$ facilitates an identification of the triplet-carrying BChl. Importantly, for these orientations, the simulations generally show signal intensities that are at least 10 times larger than for orientations with the crystal $\vec{c}$ axis parallel to B_0. In the following we will therefore limit the discussion to spectra obtained for $\vec{B}_0 \perp \vec{c}$.

To determine whether we may expect to uniquely identify the triplet-carrying molecule from the experimental triplet-EPR spectra for $\vec{B}_0 \perp \vec{c}$, we compare simulations of the triplet-EPR spectra for localization of the triplet state at different BChls. In Fig. 2, the resonant B_0 values, B_{res}, are plotted as a function of the rotation angle φ for a number of representative simulations. All simulations show the largest signal intensities in the B_0 regions where the

extreme values for B_{res}, B_{res}^{max}, are observed. The value of B_{res}^{max}, therefore, is a suitable parameter for making a first discrimination between the simulations that best represent a given experimental rotation pattern. Thus, the rotation patterns of the various simulations are classified into three groups with different value for ΔB_{res}^{max}. In ascending order of ΔB_{res}^{max}, the three groups are: a triplet state located at BChl 3 or 6, at BChl 1, 2, 4 or 5, or at BChl 7. Within these groups the differences in ΔB_{res}^{max} are significantly smaller than those between the groups.

For an overall comparison of the various simulations, we calculate the linear correlation coefficient, $r_{i,j}$, as defined in Section 1. In addition to the observation that the external short axis of the crystal may correspond to either the crystal $\vec{a}$ or the b axis, we note that the crystal $\vec{c}$ axis may coincide with either the positive or negative laboratory $\vec{y}_L$ axis. When no other misalignment of the crystal occurs, these two inherent ambiguities in aligning the crystal result in a shift of the rotation pattern: $\varphi \rightarrow \varphi \pm 90°$ or an inverted rotation sense: $\varphi \rightarrow \pm \varphi$, respectively. Considering that only the variation of the alignment angle $\Delta\varphi$ in the experiments is known, confounding the crystal $\vec{a}$ and the b axis will not result in an additional ambiguity. To account for all the possible experimental orientations of the crystal, φ is treated as a free parameter when the simulated spectra are compared, by varying the relative angle $(\varphi_i \pm \varphi_j)$ used in two simulations until a maximum correlation coefficient, $r_{i,j}$, is obtained.

In Table 1 the linear correlation coefficients between the various simulated data sets are listed. The classification into the same three groups as mentioned above is also apparent here, with all members of a particular group having a mutual correlation coefficient of at least 0.56. The data sets where a triplet state is located on either BChl 2 or BChl 5 are nearly identical: $r_{2,5} = 0.91$, while a triplet state located on BChl 7 is seen to yield an unique rotation pattern: $r_{i,7} \leq 0.5$.

The similarity between the data sets belonging to one group is only partially due to the ambiguity concerning the value of φ, related to mounting the crystals in a capillary tube. The similarity largely remains, even if the crystal would be mounted directly on the flat surface of a quartz half-rod. This follows from the maximum correlation coefficients between two data sets that have been obtained by interchanging the crystal $\vec{a}$ and b axis, and/or inverting the rotation sense. Mounting the crystal directly on the flat surface of the quartz rod only would significantly improve making a distinction between the data sets that assume a triplet state either on BChl 5 or BChl 2, while the correlation coefficients between the other data sets would remain almost identical.

We consider the effect of a possible initial misalignment of the crystal by including the angles ξ and ζ, representing the lateral and facial misalignment errors (see Fig. 1). Comparing the simulated spectra again, now with a complete parameter set φ, ξ and ζ that is optimized for a maximum correlation coefficient, we find that the correlation coefficients in Table 1 do not change noticeably when the absolute values of ξ and ζ are restricted to less than 5°, the maximum experimental misalignment (data not shown). Therefore, the numbers in Table 1 may be used for estimating how well the simulations for different triplet locations can be resolved

Table 1
Correlation coefficient $r_{i,j}$ of two simulations, assuming a triplet state localized at BChl i and j, respectively

# ^{3}BChl	2	3	4	5	6	7
1	0.56 (0.55)	0.33 (0.30)	0.65 (0.62)	0.62 (0.58)	0.31 (0.31)	0.50 (0.50)
2		0.53 (0.48)	0.65 (0.62)	0.91 (0.57)	0.53 (0.49)	0.35 (0.32)
3			0.50 (0.44)	0.51 (0.49)	0.69 (0.64)	0.24 (0.22)
4				0.62 (0.49)	0.56 (0.48)	0.33 (0.31)
5					0.42 (0.42)	0.44 (0.43)
6						0.24 (0.23)

The experimental ambiguity concerning the absolute value of the rotation angle φ has been resolved by maximalization of $r_{i,j}$ upon variation of the relative rotation angles $\Delta\varphi_{i,j}$. Values in parentheses represent the maximum correlation coefficients when this ambiguity is restricted to only a few specific orientations of the crystals (see text).

when comparing a simulated and an experimental data set, even when small experimental misalignment errors are involved.

We find that position 7, having the lowest correlation coefficients, is most easily discriminated, followed by positions 3 and 6. Positions 1, 2, 4, and 5 are strongly correlated and, given the correlation coefficient of two experimental data sets (0.78, see below), will be difficult to distinguish.

3. Results

3.1. Triplet-EPR spectra of the FMO complex in frozen solution

The triplet-EPR spectrum of the FMO complex in frozen solution is shown in Fig. 3. The EEEAAA (A = enhanced absorption, E = stimulated emission) pattern is typical for triplet state formation via intersystem crossing with p_x, $p_y \gg p_z$. The ZFS parameters match those observed with ODMR in zero-magnetic field [6] and the spectrum can be very well reproduced by a simulation as outlined in section 2.2 using $p_x = 0.41$, $p_y = 0.59$, $p_z = 0$ for the zero-field populating probabilities of the individual sublevels.

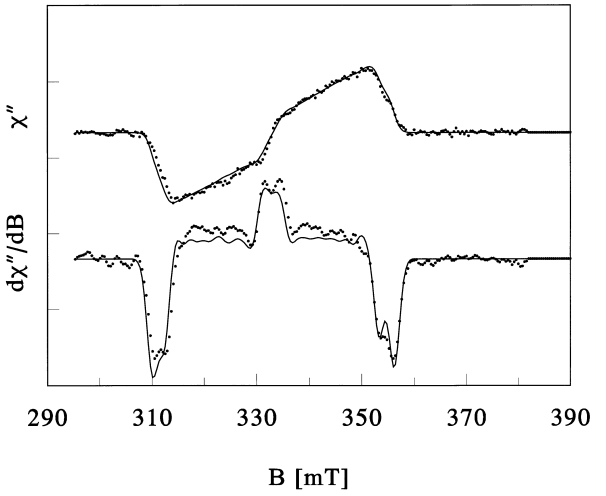

Fig. 3. Triplet-EPR spectra of the FMO complex in frozen solution. Upper trace: spectrum obtained using direct detection; lower trace: spectrum obtained using 100 kHz magnetic field modulation and 1.23 kHz light modulation. Dotted and solid lines represent the experimental and simulated spectra, respectively.

The derivative spectrum obtained with field modulation (Fig. 3) is well reproduced by numerically taking the first derivative of the simulated spectrum described above.

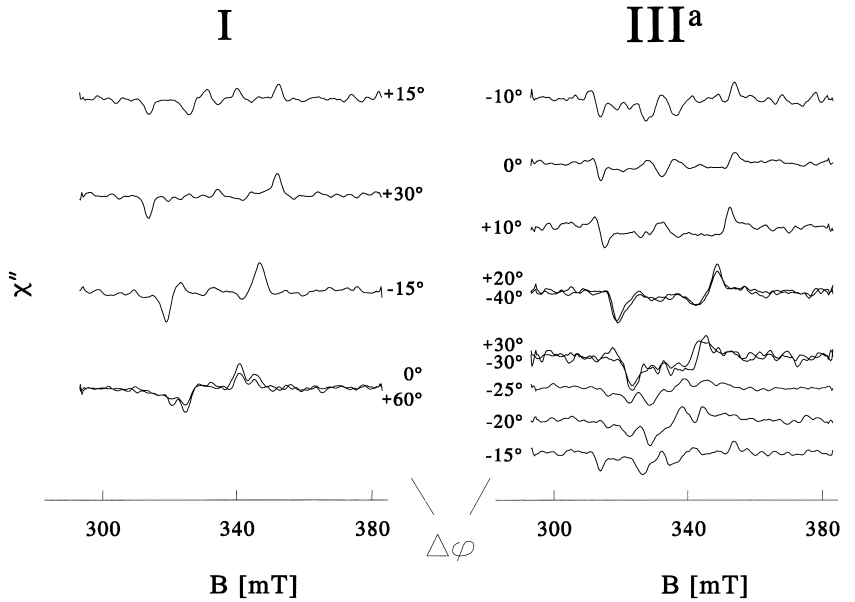

Fig. 4. Data sets I and III^a: triplet-EPR spectra of single crystals of FMO for different rotation angles φ about the crystal C_3 axis. The crystals were mounted with the C_3 axis perpendicular to the external B_0 field. Positive signals are absorptive, negative signals emissive. Note that $|\Delta\varphi(\mathrm{I,III^a})| \approx 25°$ (modulo 60°).

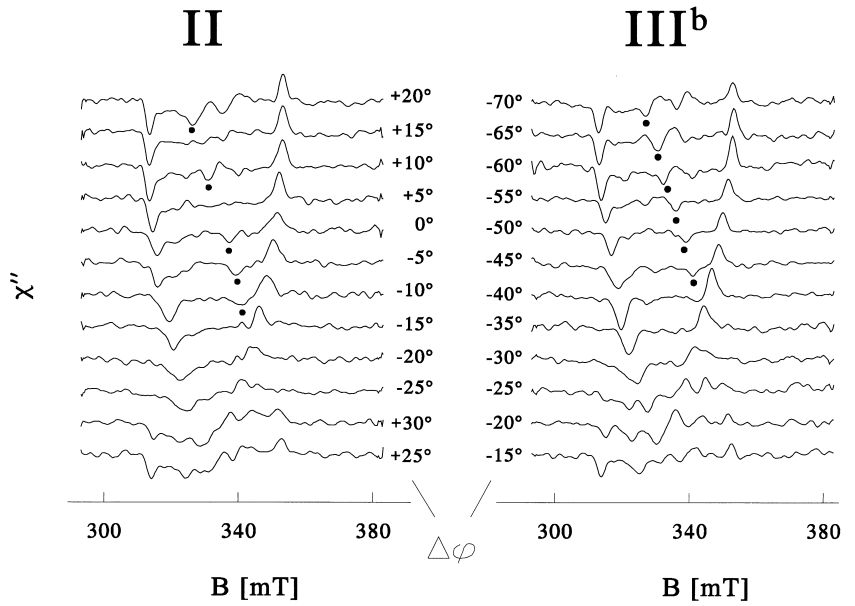

Fig. 5. Data sets II and III^b: triplet-EPR spectra of single crystals of FMO for different rotation angles φ about the crystal C_3 axis. The crystals were mounted with the symmetry C_3 axis perpendicular to the external B_0 field. For resonances indicated by dots, see text. The C_3 axes of crystal II and III^b are oriented antiparallel, resulting in an inverted rotation sense of the two data sets: $|\Delta\varphi(\mathrm{II})+\Delta\varphi(\mathrm{III}^b)| \approx 50°$ (modulo 60°).

3.2. Triplet-EPR spectra of single crystals of the FMO complex

The experiments on single crystals of the FMO complex were performed on three different crystals, labeled I, II and III. The experiments on crystal III were carried out in two separate sessions including a complete freeze-thaw cycle of the cryostat and remounting the crystal between the experimental sessions. The data sets corresponding to the various experiments are denoted I, II, III^a and III^b, respectively, and are plotted in Figs. 4 and 5. The traces that correspond to a similar orientation of the different crystals have been plotted with the same offset. The most comprehensive data sets, II and III^b, consist of 12 crystal orientations in steps of $\Delta\varphi = 5°$ around the laboratory $\vec{y}_L$ axis, yielding a complete rotation period of 60°. Although the EPR signals are small and require substantial averaging, the characteristic experimental features of the various spectra reproduce well, both for different crystals and for the data sets III^a and III^b. Furthermore, we note that rotation of a crystal over 60° around the symmetry axis of the crystal, reproduces the original trace. (Compare the traces measured at $\varphi = (0°, 60°)$ of data set I, and $\varphi = (-30°, 30°)$ and $(-40°, 20°)$ of data set III^a in Fig. 4.) Thus, we may conclude that the observed signals are not due to artifacts such as crystal defects, and that the crystals are not deteriorated by the prolonged exposure to high intensity illumination, necessary to detect the small triplet-EPR signal.

After optimization of the overlap of two given experimental data sets by varying the mutual difference in rotation angle $\Delta\varphi_{A,B}$, we find that the average correlation coefficient between the experimental data sets is (0.69 ± 0.06). For the most comprehensive data sets II and III^b, we find $r^{\max}_{\mathrm{II,III}^b} = 0.78$. Assuming that the crystal $\vec{c}$ axes are perfectly aligned along the laboratory $\vec{y}_L$ axis (see also below), and that other systematic errors, such as crystal defects, do not play an important role, the fraction $\sqrt{(1-r^{\max})}$ represents random noise in the experiments. Thus, $r_{\max}$ puts an upper limit to the maximum achievable correlation between an experimental data set and a particular simulation, given the present signal-to-noise ratio.

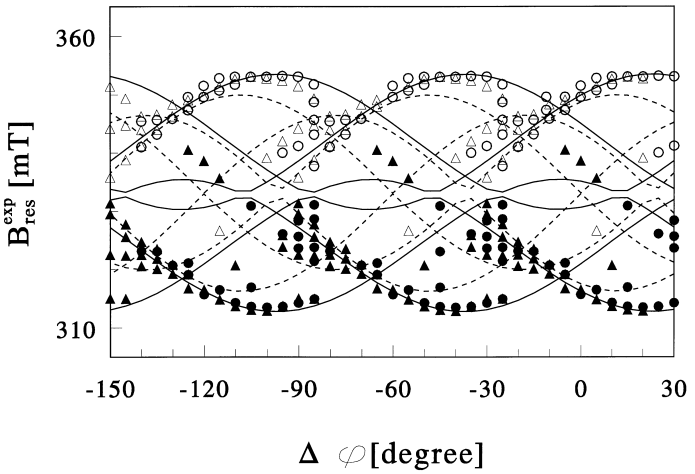

Fig. 6. Resonant B_0 values plotted as a function of the rotation angle φ for experimental data sets II (circles) and III^b (triangles). Closed and open markers represent emissive and absorptive EPR signals, respectively. Solid and broken lines represent resonant B_0 values resulting from a simulation with localization of the triplet state on either BChl 1 or 3, respectively.

4. Discussion

4.1. The FMO complex in frozen solution

The triplet-EPR spectrum of the FMO complex in frozen solution obtained by direct detection as well as the derivative spectrum obtained by CW-EPR and field modulation can be reproduced very well by the simulation procedure discussed in Section 1, assuming that the population differences of the triplet sublevels are determined by the differences between the initial population probabilities only, neglecting triplet decay and microwave-induced or spin lattice relaxation. In principle, the intensities in the field modulation (derivative) spectrum should depend on the decay rates of the triplet sublevels. Considering the similarity of the direct detection spectrum and the field modulation spectrum, we conclude that all triplet sublevels are effectively (de-)populated with the *same* (spin lattice or microwave-induced) relaxation rate. This conclusion is consistent with the observation that the relative intensities in the derivative spectrum do not change between 20 K and 100 K (data not shown), and is confirmed by the observation that for optimal signal-to-noise ratio, the second boxcar gate for the direct detection method must be close (10 μs) to the laser flash. In other words, leveling of the population difference at the temperature of the sample immediately after the laser flash is much faster than expected on the basis of the depopulation rates observed at 1.2 K for BChl *a* in methyltetrahydrofuran [23]. This observation suggests that in the lower temperature range the temperature of the crystal immediately after excitation is considerably higher than the environmental (cryostat) temperature.

4.2. Single crystals

For comparing the experimental and simulated spectra the experimental traces of data sets II and III^b were first fitted with a minimum number of Gaussian bands. A linewidth of 2.25 mT (FWHM), which was observed for a number of isolated transitions in the experimental spectra, was used as the common linewidth for all Gaussian bands. The central values of the Gaussian bands, B_{res}^{exp}, are plotted as function of the rotation angle φ in Fig. 6, distinguishing between emissive and absorptive EPR signals. For clarity, in Fig. 6 only B_{res} values are plotted that correspond to experimental signal amplitudes larger than 33% of the maximum signal amplitude.

The B_{res} values resulting from simulations for a triplet localized at BChl 1, 2, 4, or 5 show a better overlap with experimental values than those resulting from simulations for a triplet localized at BChl 3, 6 or 7. By way of example, in Fig. 6 the simulated B_{res} values for a triplet localized at BChl 1 or at BChl 3 are plotted as a function of the rotation angle φ. To obtain more resolution in identifying the triplet-carrying molecule, we have calculated the maximum lin-

ear correlation coefficients between various simulations and an averaged experimental data set, which was obtained by first optimizing the overlap between data sets II and III[b] as described above, and then averaging the two data sets. From the correlation coefficients listed in Table 2, we conclude that the averaged experimental data set is best reproduced by assuming a triplet state either located on BChl 1 ($r_{max} = 0.608$), or BChl 5 ($r_{max} = 0.616$).

The correlation coefficients for the two best fits are somewhat lower than the correlation coefficient between the experimental data sets II and III[b] ($r = 0.78$). This lower correlation is caused by the following differences between the experimental data and the simulated data sets:

- At least 8 Gaussians are needed to adequately fit most experimental spectra, although we expect a maximum of six resonances in the individual spectra (Figs. 4 and 5).
- When the rotation pattern of simulated resonant B_0 values for a triplet localized at BChl 1, 2, 4, or 5 is compared with that of the averaged experimental data set, several resonances with more than 80% of the maximum signal intensity in the simulation are not observed in the experiment.
- All simulations mainly predict absorptive (emissive) signals at B_0 values above (below) centerfield. In both experimental data sets, however, a number of emissive (absorptive) resonances above (below) centerfield seem to be present, which have too much intensity (up to $\sim$40% of the maximum signal amplitude) to be regarded as noise, and appear to be related to emissive (absorptive) resonances below (above) centerfield (see for example the dots in Fig. 5). An intensity pattern reversed in sign for a single triplet state localized at BChls 1, 6, or 7, can only be reproduced for a very limited number of resonances near centerfield, by assuming unrealistic zero-field population probabilities. A simulation of the triplet-EPR spectra for the FMO complex in frozen solution with such values for the population probabilities yields large discrepancies with the experimental spectrum (data not shown).

Table 2
Maximum correlation coefficient r between a simulated data set for a triplet state localized at the various BChl sites 1–7, and the averaged experimental data set (II+III[b]), obtained upon optimization of the overlap of the two data sets (see text)

# ^{3}BChl	r	φ_{III^b}
1	0.61	35°
2	0.57	75°
3	0.55	35°
4	0.59	5°
5	0.62	70°
6	0.52	5°
7	0.41	0°

To account for the aforementioned differences between simulation and experiment, we tested two hypotheses:

1. The crystal $\vec{c}$ axis is not perfectly aligned along the laboratory $\vec{y}_L$ axis prior to rotating the crystal around this axis. The misalignment of the crystal is defined by the angles ξ and ζ in Fig. 1.
2. There are two triplet states, located at two different BChls.

(1) *Misalignment of the crystal*

When the crystal is not perfectly aligned with the crystal $\vec{c}$ axis along the laboratory $\vec{y}_L$ axis prior to an experiment (hypothesis 1), the two BChls that have the same orientation with respect to $|\vec{B}_0|$ when the crystal $\vec{c}$ axis is perfectly aligned along the laboratory $\vec{y}_L$ axis (see Section 1), will have a magnetically inequivalent orientation. This misalignment increases the maximum number of resonances that can be observed in a particular spectrum from 6 to 12. Inclusion of two additional degrees of freedom, ξ and ζ (see Fig. 1), results in a higher maximum correlation coefficient. The correlation coefficient is found using a Marquart-Levenberg search routine to optimize the overlap between the data sets. Note that orientation of the crystal $\vec{c}$ axis along either the positive or negative laboratory $\vec{y}_L$ axis is not equivalent to inversion of the rotation sense, when the crystal $\vec{c}$ axis is not perfectly aligned parallel to the laboratory $\vec{y}_L$ axis. Several (local) maximum r values exist upon varying the initial assumptions concerning the rotation sense or mounting direction of the crystal. Therefore, the optimization was repeated for all the possible experimental crystal orientations. The result is that only for a triplet

Table 3
Maximum correlation coefficient r between a simulated data set for two triplet states localized at two different BChl sites, and the averaged experimental data set (II+III^b), obtained upon optimization of the overlap of the two data sets (see text)

# ^{3}BChl	r	φ_{III^b}
1+3	0.72	35°
1+5	0.68	30°
5+6	0.68	10°
5+2	0.66	15°
3+4	0.66	0°

For the simulations it was assumed that the two different BChls have equal probability of triplet formation.

state localized at BChl 5 or at BChl 6, correlation coefficients for both experimental data sets are obtained that are higher than those obtained for perfect alignment of the crystal ($r = 0.68 \pm 0.01$ and $r = 0.65 \pm 0.01$, respectively). For these higher correlation coefficients, however, the misalignment angles ξ and/or ζ are significantly larger than 5°, the maximum estimated experimental misalignment. We therefore we reject the hypothesis that crystal misalignment is the origin of the difference between experimental and simulated data sets.

(2) *Two triplet states*

For simplicity, we only consider an *equal* probability of finding a triplet state at two BChls. An additional triplet state may be created at trimers containing already one triplet state within the time span of a single optical excitation pulse. Double excitation of the FMO complex has been observed earlier (E.M. Franken, S. Neerken, T.J. Aartsma, unpublished results) and cannot be excluded at the relatively high excitation densities necessary to observe the small triplet-EPR signal. Alternatively, the singlet excited state does not localize at the one particular BChl that dominates the lowest excited state, and due to local temperatures above thermal equilibrium (see also above), is spread over the lowest and second lowest excited states. According to [7], intersystem crossing would then predominantly occur at two BChl sites (BChl 3 and BChl 1, see also below). The energy difference between the lowest and second-lowest excited states, however, corresponds to $\sim$110 K, making this alternative highly unlikely.

The correlation coefficients that are obtained at maximum overlap between the averaged data set (II+III^b) and the sum of two simulations for two distinct BChl sites are listed in Table 3. Assuming an equal percentage of the triplet states located on BChls 1 and 3 in particular, a significant improvement of the correlation between simulation and experiment is obtained: $r_{max} = 0.72$. When an equal percentage of the triplet states is assumed to be located at BChls 1 and 5 or at BChl 5 and 6, a smaller correlation coefficient is obtained: $r_{max} = 0.68$. *If* it is possible to create a second triplet state in a subunit of the FMO complex, then localization of a second triplet state at BChl 1 would agree with the simulation of the optical steady-state spectra of the FMO complex using the exciton model presented in [7]. In this model the excited states of the FMO complex are described by a linear combination of the individual monomer BChl excited states. Generally, the probability of finding a triplet state at a particular BChl is proportional to its contribution to the dipole strengths of thermally accessible transitions after thermal equilibration of the excitation energy. In the best simulation of the optical steady-state spectra, the two lowest excited states mainly contain contributions of BChl 3 and 1, respectively: BChl 3 contributes $(0.995)^2 \times 100\% = 99.5\%$ of the total dipole strength to the lowest excited state, while BChl 1 contributes $(0.845)^2 \times 100\% = 84.5\%$ to the dipole strength of the second-lowest state in the manifold. As a result the contributions of the various BChls to the other 6 exciton states (including the second-lowest excited state) remain almost unchanged after triplet formation at BChl 3 (see Table 4 in [7]). Therefore, it might be expected that a second triplet state will be formed predominantly at BChl 1. Note, however, that the distance in energy between the second- and the third-lowest exciton states is small enough ($\sim$19 K) for further delocalization of the excitation by thermal activation. Hence, when two photons are absorbed, there may be a significant contribution of other BChls to the triplet-EPR spectrum. It follows that assuming an *equal* probability for finding a triplet state at two BChl sites is too simple a model for describing creation of secondary triplet states under the experimental conditions. Without accurate data on sample temperature immediately after excitation, however, further refinement does not seem warranted.

5. Conclusions

We obtained triplet-EPR spectra of single crystals of the FMO complex of *Prostecochloris aestuarii*. Although the signal amplitudes are small, the spectra reproduce for different crystals as well as for experiments on the same crystal in a second experimental session. Furthermore, the spectra reproduce when the crystal is rotated over 60° around the C_3 axis of the crystal, indicating that the crystals are well ordered. Two triplet states, localized at two different sites (BChl 3 and BChl 1) give the best overall fit of the data. This result corresponds well with the interpretation of the optical steady-state spectra, which shows that the lowest and second-lowest exciton states are dominated by contributions of BChls 3 and 1, respectively. Thus, our experiments show that single-crystal EPR on the FMO complex provides an independent tool for the identification of the BChls contributing predominantly to the lowest excited states. We expect that future work with 2 or 3 mm EPR, possibly in combination with echo-detection, will result in considerable enhancement of the sensitivity at low optical excitation power. Then, creation of secondary triplet states is minimized, and the BChl associated with the lowest exciton state may be unambiguously identified.

We note that our assignment of BChl 1 and 3 as the lowest-energy BChls differs radically from an assignment based on quantum-chemical calculations [24]. This difference may be (partly) due to the difference in temperature (for the calculations the room-temperature crystal structure was used) and the sensitivity of the calculated energies to the precise configuration of the BChls.

Acknowledgements

Christof Francke skilfully isolated the FMO complexes for experiments on randomly oriented samples. The investigations were supported by the Life Science Foundation (SLW) and by the Foundation for Chemical Research (SON), both financed by the Netherlands Organization for Scientific Research (NWO), and by the EU (Contract FMRX-CT96-0081).

References

[1] J.M. Olson, in: R.K. Clayton, W.R. Sistrom (Eds.), The Photosynthetic Bacteria, Plenum Press, New York, 1978, pp. 161–178.
[2] D.E. Tronrud, M.F. Schmidt, B.W. Matthews, J. Mol. Biol. 188 (1986) 443–454.
[3] F. van Mourik, R.R. Verwijst, J.M. Mulder, R. van Grondelle, J. Phys. Chem. 98 (1994) 10307–10312.
[4] K.D. Philipson, K. Sauer, Biochemistry 11 (1972) 1880–1885.
[5] H. Vasmel, T. Swarthoff, H.J.M. Kramer, J. Amesz, Biochim. Biophys. Acta 725 (1983) 361–367.
[6] R.J.W. Louwe, J. Vrieze, A.J. Hoff, T.J. Aartsma, J. Phys. Chem. 101 (1997) 11273–11279.
[7] R.J.W. Louwe, J. Vrieze, T.J. Aartsma, A.J. Hoff, J. Phys. Chem. 101 (1997) 11280–11287.
[8] R.M. Pearlstein, Photosynth. Res. 31 (1992) 213–226.
[9] X. Lu, R.M. Pearlstein, Photochem. Photobiol. 57 (1993) 86–91.
[10] D. Gülen, J. Phys. Chem. 100 (1996) 17683–17689.
[11] P. Gast, M.R. Wasielewski, M. Schiffer, J.R. Norris, Nature 305 (1983) 451–452.
[12] P. Gast, J.R. Norris, FEBS Lett. 177 (1984) 277–280.
[13] D.E. Budil, S.S. Taremi, P. Gast, J.R. Norris, H.A. Frank, Israel. J. Chem. 28 (1988) 59–66.
[14] T.D. Sterling, S.V. Pollack, Introduction to Statistical Data Processing, Prentice-Hall, Englewood Cliffs, NJ, 1968.
[15] S.P. McGlynn, T. Azumi, M. Kinoshita, Molecular Spectroscopy of the Triplet State, Prentice-Hall, Englewood Cliffs, NJ, 1969.
[16] M.K. Bosch, I.I. Proskuryakov, P. Gast, A.J. Hoff, J. Phys. Chem. 100 (1996) 2384–2390.
[17] M. Miller, R.P. Cox, J.M. Olson, Photosynth. Res. 41 (1994) 97–103.
[18] R.E. Fenna, B.W. Matthews, J.M. Olson, E.K. Shaw, J. Mol. Biol. 84 (1974) 231–240.
[19] P. Kottis, R. Lefebvre, J. Phys. Chem. 39 (1963) 393–403.
[20] A.M.P. Ros, Ph.D. Thesis, Leiden University, The Netherlands, 1991.
[21] H. Vasmel, H.J. den Blanken, J.T. Dijkman, A.J. Hoff, J. Amesz, Biochim. Biophys. Acta 767 (1984) 200–208.
[22] O. Burghaus, M. Plato, D. Bumann, B. Neumann, W. Lubitz, K. Möbius, Chem. Phys. Lett. 185 (1991) 381–386.
[23] H.J. den Blanken, R.F. Meiburg, A.J. Hoff, Chem. Phys. Lett. 96 (1983) 343–347.
[24] E. Gudowska-Nowak, M.D. Newton, J. Fajer, J. Phys. Chem. 94 (1990) 5795–5801.